Design Study for Multifunctional 3D Re-entrant Auxetics

*Stefan Bronder, Franziska Herter, Anabel Röhrig, Dirk Bähre, and Anne Jung**

The increasing demands of safety, cost reduction, or weight reduction on components call for new, multifunctional materials. Mechanical metamaterials, such as auxetic materials, provide enhanced properties due to a specially tailored microstructure. The negative Poisson's ratio of auxetics, for instance, increases the impact and thermal shock resistance. Herein, a parametrized model of a modified auxetic structure is simulated using the finite-element software ABAQUS. Three out of five geometry parameters are varied between a minimum and maximum value to establish their impact on the energy absorption capacity and the Poisson's ratio using design of experiment (DoE). All eight resulting structures are additively manufactured by selective laser melting (SLM) and experimentally investigated under uniaxial compression to validate the simulations. The size of a unit cell has the biggest impact on both target values. Energy absorption capacity and Poisson's ratio are directly competing in optimization; hence, a compromise is necessary. The quasistatic compression experiments verify the simulation results up to the first collapse. Afterward, the specimens are brittle, which is not accounted for in the simulations, and this may result from the high process complexity of SLM manufacturing.

1. Introduction

Auxetic structures are a subclass of mechanical metamaterials with the governing property of a negative Poisson's ratio. Therefore, such materials expand laterally to the tensile direction.[1] Other properties derived from this, are an increased thermal shock resistance,[2] a higher fracture toughness,[3,4] and indentation resistance.[5–7] Hence, auxetic materials are suitable for ballistic and blast protection[8–11] or as crash absorbers due to increased energy dissipation.[12,13] For those applications, the

S. Bronder, A. Jung
Applied Mechanics—Foams and Metamaterials
Saarland University
Campus C6.3, 66123 Saarbrücken, Germany
E-mail: anne.jung@mx.uni-saarland.de

F. Herter, A. Röhrig, D. Bähre
Institute of Production Engineering
Saarland University
Campus A4.2, 66123 Saarbrücken, Germany

(iD) The ORCID identification number(s) for the author(s) of this article can be found under https://doi.org/10.1002/adem.202100816.

dynamic loading case is of special interest[14–16] as well as a lightweight approach through truss structures[17] or hybrid materials. Bronder et al.[18] electrochemically coated a printed polymeric auxetic structure with a thin layer of nickel and were able to improve properties such as plastic collapse stress (PCS) or plateau stress and thus also the energy absorption capacity.

Additional applications of auxetics are press-fit fasteners,[19] stents, arterial prosthesis,[20] or sport-protective equipment.[21] Also, fiber-reinforced composites make use of the auxetic effect, either through a suitable stacking sequence of the fiber layers,[22,23] thereby increasing the low-velocity impact resistance and showing a more localized initial damage,[24] or with auxetic fibers inside the polymer matrix,[25] which increases the fiber pull-out resistance. Both variants counteract the two common failure mechanisms of composite materials.

Even though mechanical metamaterials are designed, artificial materials, the auxetic effect can also be found in nature, for example, in some cubic crystal lattices[26] or some forms of skin.[27–29] The first manufactured auxetic foam, however, was produced by Lakes et al.[6] Through triaxial compression in combination with heating, they were able to convert a conventional polyurethane foam to an auxetic one. Thereby, they marked a starting point for the investigation of auxetic materials to exploit their high tailoring potential. Today, auxetics have been developed across all material classes and sizes, even down to a molecular level.[30]

How the microstructure for auxetic behavior works is easiest explained for a 2D case (**Figure 1**). Almgren[31] was the first to describe the re-entrant honeycomb structure as a possibility to display a negative Poisson's ratio. Also rotating rigid bodies[32] with connecting hinges at their corners, such as rectangles, triangles, and so on, are a possibility to achieve an auxetic effect. More recent microstructures with auxetic properties are chiral lattices[33–36] or double-arrowhead structures[37] (Figure 1b). To enhance the energy absorption capacity of the auxetics, an additional half strut can be added in the middle of the unit cell.[38] This increases the stability after initial deformation as well as preserves the auxetic effect and its benefits, thus creating a multifunctional auxetic structure applicable to many crash absorber and protection devices.
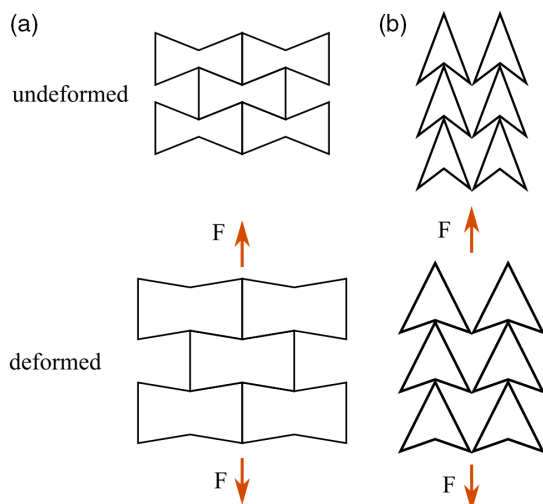
With the improvement of additive manufacturing (AM) capabilities, complex structures are much easier to produce and test. Selective laser melting (SLM), developed in 1998,[39] is a possibility to manufacture 3D structures out of metal. SLM is a powder bed fusion process with a laser as power source, where selected regions of metal powder are melted down and thereby fused

ADVANCED
SCIENCE NEWS
www.advancedsciencenews.com

ADVANCED
ENGINEERING
MATERIALS
www.aem-journal.com

Figure 1. 2D deformation schematics of auxetic microstructures: a) re-entrant honeycomb and b) double arrowhead.

together. The 3D model of the product is usually created with a computer-aided design (CAD) software and exported to a surface tessellation language (STL) file, through approximation of the surface with triangles. 2D slices are then created from the 3D model and sent to the AM device to produce the specimen.[40]

For use in lightweight construction, all specimens of this contribution were produced with SLM out of aluminum, which is one of the less-commonly used powder metals. The main research is done on iron, titanium, and nickel as those have widespread applications.[41] The usual layer resolution of the SLM process ranges from 20 to 100 μm,[41] which is not as good as the resolution for, for example, polyjet printing.[42] However, SLM produces many fabrication defects, leading to a weakening of the product.[43–45] For more detailed information on the SLM process, the reader is referred to the literature.[41]

All specimens of this contribution were evaluated with finite-element analysis (FEA) of a parametrized model. To establish a better understanding of the behavior in relation to the geometry parameters by means of design of experiment (DoE), a full-factorial testing plan was used. This testing plan reduces the amount of experiments by mapping all possible combinations of the parameters in a factorial space.[46] So, for example, with three parameters varied on two levels, a cube in the factorial space is constructed. Each of the eight edges represents a possible combination and thereby one experiment. The main effects of the single factors are calculated as the difference between the mean values of the two levels. The slope of the straight line between the two points indicates the influence magnitude of a specific factor. To establish the interaction between single factors, the prefactors of the levels are multiplied and then averaged. The results are two straight lines with the slope difference as a measure for the magnitude of the interaction.

2. Experimental Section

The specimens in the present contribution were all variants of the same parametrized unit cell (**Figure 2**), taken from the
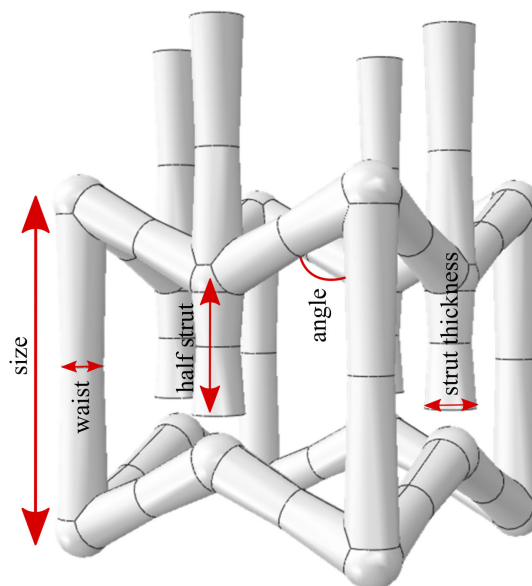
Figure 2. Modified auxetic unit cell with the five defined geometry parameters.

literature.[38] For the factorial testing plan only waist, strut thickness, and size were investigated with a constant re-entrant angle and half strut. All variants were simulated with ABAQUS and experimentally investigated under compressive loading conditions.
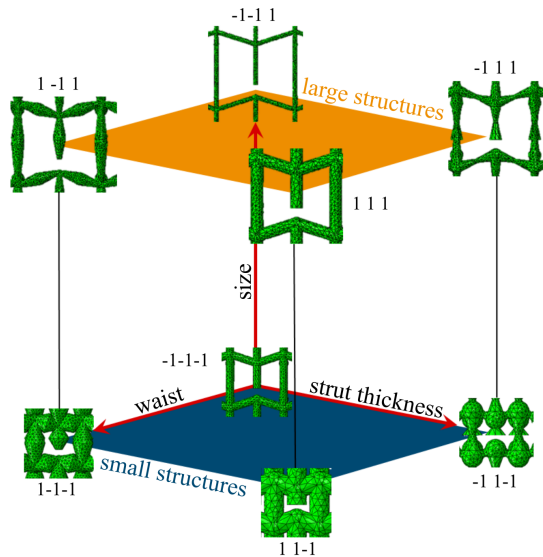
2.1. Factorial Testing Plan

To reduce the amount of specimens, only three out of five geometry parameters were considered for the 2^3-full-factorial testing plan, resulting in eight different parameter combinations. In factorial space, this resembled a cube with one specimen on each edge (**Figure 3**).

As a linear approximation was assumed, all three geometry parameters were varied between a minimum (min) and a maximum (max) value. The respective values are shown in **Table 1**. The max values were selected because of the building space of the SLM machine, and those were the biggest specimens producible, whereas the min values were the smallest sensible measures. Smaller values would have lead to a too fragile structure and would also have been too difficult to manufacture.

Finite element (FE) simulations and compression experiments were conducted for all eight resulting microstructures. Finally, the 2^3-full-factorial testing plan was evaluated regarding the two target values energy absorption capacity and Poisson's ratio. The Poisson's ratios were only calculated within the pseudoelastic regime before the highly nonlinear effects came into play, to neglect the strong variations at high strain levels.
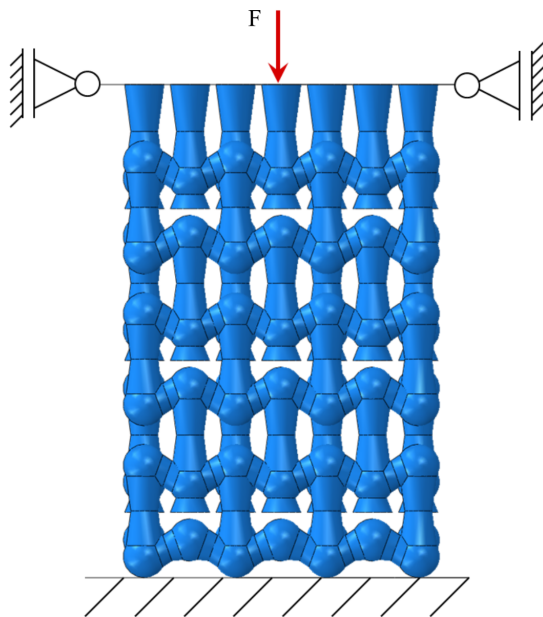
2.2. FE Simulations

Every structure was modeled using the FE software ABAQUS**** and scripted with Python for pre- and postprocessing. The simulated compression experiment (**Figure 4**) was conducted until 33% strain to gain a good estimate of the plateau stress but reduce computational time.

2100816 (2 of 10)

**ADVANCED
SCIENCE NEWS**

www.advancedsciencenews.com

**ADVANCED
ENGINEERING
MATERIALS**

www.aem-journal.com

Figure 3. All eight resulting unit cells for the variations of the three geometry parameters in factorial space.

Table 1. Minimum and maximum values for the geometry parameters varied within the full-factorial testing plan.

	Waist [mm]	Strut thickness [mm]	Size [mm]
Min (−1)	0.5	0.5	7
Max (1)	1.5	1.5	20

Figure 4. Simulation setup for the compression experiments with boundary conditions.

As there were highly nonlinear deformations, the explicit solver was used. This, in combination with the complex structure of the specimen, led to the usage of tetrahedral elements with a modified formulation (C3D10M). To model the compression experiment, the specimens were placed between two rigid plates. One plate was fixed while the other one moved downwards like in a real uniaxial compression experiment. An ABAQUS general contact was used to model the contact behavior. Herein, the pure master−slave procedure enforces contact constraints using a penalty procedure by detecting node-into-face and edge-into-edge penetrations. The interaction penalty was implemented as Coulomb friction with a 0.1 friction coefficient for tangential behavior. As a material model, a simple elastic−plastic material model with a plastic table was used. The material data was based on uniaxial tensile tests of SLM aluminum, manufactured in three different orientations. A mesh study was conducted in a previous work.[18]

2.3. Selective Laser Melting

The specimens of the tensile tests as well as the structures of the testing plan were produced on SLM 125 machine (SLM Solutions Group AG, Lübeck, Germany). The process parameters used for the structures are shown in **Table 2**. Two different types of filling strategies were used because "total fill" yielded better manufacturing qualities for thin struts, whereas "hatch" produced a better surface for thick struts. In particular, the specimens were produce from AlSi10Mg metal powder (SLM Solutions Group AG, Lübeck, Germany) as raw material, which was evenly distributed on a flat substrate plate. The powder was then exposed to a laser at defined positions, thereby melting the laser-exposed powder particles and causing them to bond with each other in the liquid phase. Afterward, the molten material solidified again. The substrate plate was then lowered by the defined layer thickness (Table 2). These three steps, powder application−laser exposure−lowering of the plate, were conducted repeatedly until the component was completely manufactured. The whole process was conducted in argon atmosphere.

The specimens on the substrate plate were subjected to heat treatment afterward. For this purpose, the specimens were kept in the oven at 300 °C for 2 h and then cooled naturally. Thereafter, the specimens were separated from the substrate plate and support structures were removed manually due to the complex structure. Then, the specimens were cleaned in an ultrasonic bath to get rid of all the remaining powder particles

Table 2. Process parameters for the SLM manufacturing process; "hatch" means stripes as fill pattern; and "total fill" means a circular fill pattern for the slices.

Process parameter [unit]	Value
Laser wavelength [nm]	1064
Laser power [W]	250
Scan speed [mm s^{-1}]	2000
Layer thickness [μm]	30
Laser hatch distance [mm]	0.114
Scanning strategy:	
Strut thickness 1.5 mm	"hatch"
Strut thickness 0.5 mm	"total fill"
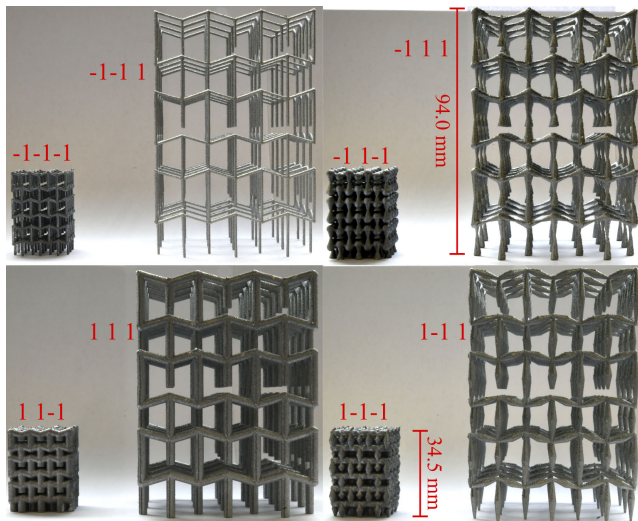
Figure 5. SLM-manufactured specimens for all geometry parameter sets. 1 and −1 denote the max. and min. value of the three geometry parameters waist, strut thickness, and size, respectively, as shown in Figure 3 (left: small structures and right: corresponding large structure).

Table 3. Mean size and mass of the manufactured specimens per type.

	Waist [mm]	Strut thickness [mm]	Size [mm]	Length [mm]	Width [mm]	Height [mm]	Mass [g]
Small	0.5	0.5	7	22.3	22.4	33.4	3.85
	1.5	0.5	7	24.0	24.1	34.5	17.36
	1.5	1.5	7	24.2	24.5	34.3	26.93
	0.5	1.5	7	24.2	24.6	34.5	14.66
Large	0.5	0.5	20	61.6	61.7	94.1	11.27
	1.5	0.5	20	63.0	63.1	93.3	48.55
	1.5	1.5	20	63.4	63.5	93.3	97.82
	0.5	1.5	20	63.2	63.7	95.2	42.89

and made ready for the compression experiments (**Figure 5**). The measures of the specimens are shown in **Table 3**.

2.4. Uniaxial Experiments

All compression (structures) and tensile (dog-bone, dimensions (L [mm] × W [mm] × T [mm]) 40 × 5 × 2.5) experiments were conducted using the universal testing machine ElectroPuls E10000 (Ltd. Instron, Pfungstand, Germany) with a strain rate of 0.003 s^{-1}. For an evaluation with digital image correlation (DIC), all experiments were observed with two 9 megapixels charged coupled device (CCD) cameras (Manta G-917B, Allied Visions Technologies GmbH, Puchheim, Germany). Also, all specimens were primed white and an irregular, black speckled pattern was applied for the DIC. The frame rate of the two cameras was coupled to the testing machine to trigger an image at every 0.5% strain. The commercial software ISTRA4D**** (Dantec Dynamics, Skovlunde, Denmark) was used to conduct DIC.

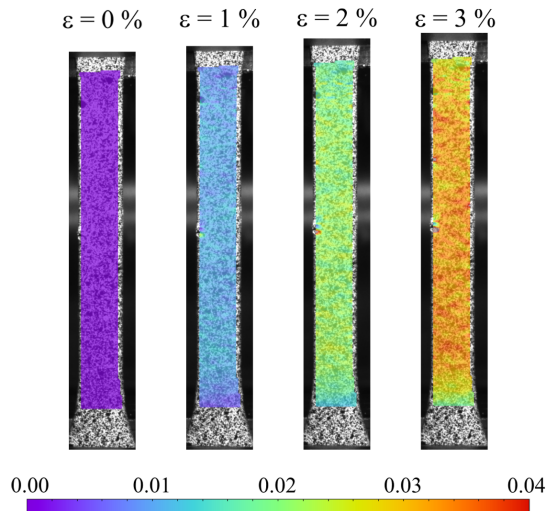## 3. Results

3.1. SLM Aluminum Tensile Tests

The preceding tensile tests on SLM aluminum from the same SLM machine as all other specimens were conducted to calibrate the material model for the FE simulations. From the stress−strain diagrams (**Figure 6**), a mean Young's modulus of 62.27 GPa was measured. The plastic region was approximated with 20 points as a plastic table, extracted from the stress−strain diagram with ABAQUS. 0°, 45°, and 90° denote the angles between the substrate plate of the SLM machine and the length axis of the dog-bone specimens. The specimens which were flat on the substrate plate (0°) are more brittle and have a lower elastic limit than the other two manufacturing directions. Within one production batch, the deviation is extremely small. All specimens are flat tensile specimens according to DIN EN ISO 6892-1.[47] The behavior during tension is similar for all three variants of the specimens. **Figure 7** shows the tensile deformation exemplary for a 0°-dog-bone specimen measured with DIC. There is a uniform strain over the entire specimen regardless of the angle between specimen length axis and substrate plate of the SLM device.

3.2. Simulation

The FE simulations yield the stress−strain behavior for the eight different parameter sets of the factorial testing plan (**Figure 8**). Within the geometry space, a wide stress−strain relation range is covered. For an optimization of the energy absorption capacity, the area beneath the curves is calculated. Also for lightweight purposes the energy absorption capacity results are normalized on the total mass of the model. All results are shown in **Table 4**. As the aim is to achieve a good compromise between energy absorption capacity and Poisson's ratio, a small structure with
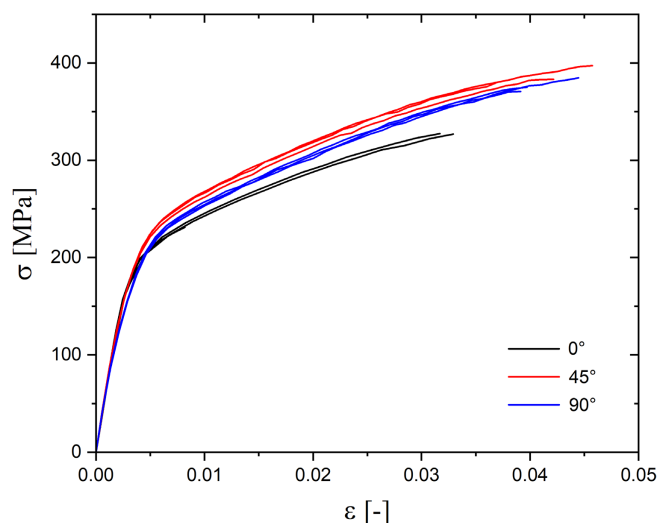
Figure 6. Stress−strain diagrams of SLM flat dog-bone tensile specimens. 0°, 45°, and 90° are the angles between specimen length axis and substrate plate of the SLM device.

Figure 7. DIC measurement of a 0°-dog-bone specimen at certain global strain values.

Table 4. Calculated mass specific energy absorption capacity E and Poisson's ratio ν from the simulations. 1 and -1 denote the max and min values of the three geometry parameters waist, strut thickness, and size, respectively. Green is the best compromise for both target values.

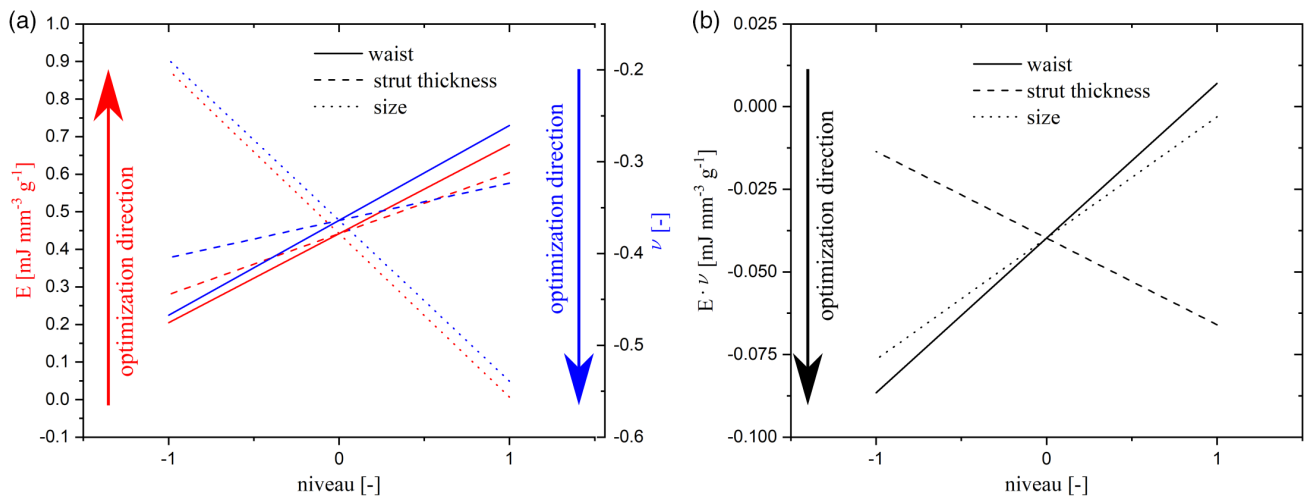|	Parameter level	E [mJ mm^{-3} g^{-1}]	ν [–]
Small	$-1-1-1$	0.2199	-0.33
	$1-1-1$	0.8933	0.03
	$1\ 1-1$	1.8009	0.01
	$-1\ 1-1$	0.5941	-0.45
Large	$-1-1\ 1$	0.0030	-0.64
	$1-1\ 1$	0.0024	-0.67
	$1\ 1\ 1$	0.0026	-0.44
	$-1\ 1\ 1$	0.0188	-0.41

waist struts yields the best result (Table 4 green). In addition, a wide range of possible Poisson's ratios is achievable within the geometry space. While the large structures yield very low specific energy absorption capacities, they all display a high auxetic effect. In contrast, the small structures provide a significantly higher energy absorption capacity.

From the evaluation of the simulations, the effects of each geometry parameter on the two target values of the factorial testing plan can be approximated linearly. The goal is to maximize the energy absorption capacity while achieving a negative Poisson's ratio as low as possible. The effect plots (**Figure 9**a) illustrate the opposing impact of the geometry parameters on the two target values. The slope of the straight lines between

the min (-1) and max (1) values indicates the strength of a single geometry parameter on the target value. Consequently, the unit cell size has the biggest impact on both the energy absorption capacity and the Poisson's ratio. Waist and strut thickness have a much lower effect, with the waist having the second biggest impact. Furthermore, an increase in unit cell size has the opposite effect on the two target values compared with an increase in waist or strut thickness. The interaction plots between the geometry parameters only showed that waist and unit cell size have the biggest interaction for both target values. However, this is already clear, as those two geometry parameters are the two most influential on both target values. To achieve the best compromise, an optimization of the product of energy absorption capacity and Poisson's ratio is a first simple approach (Figure 9b). Here, the waist has the biggest impact on the optimization target, followed by unit cell size, and then strut thickness as the least influential value.
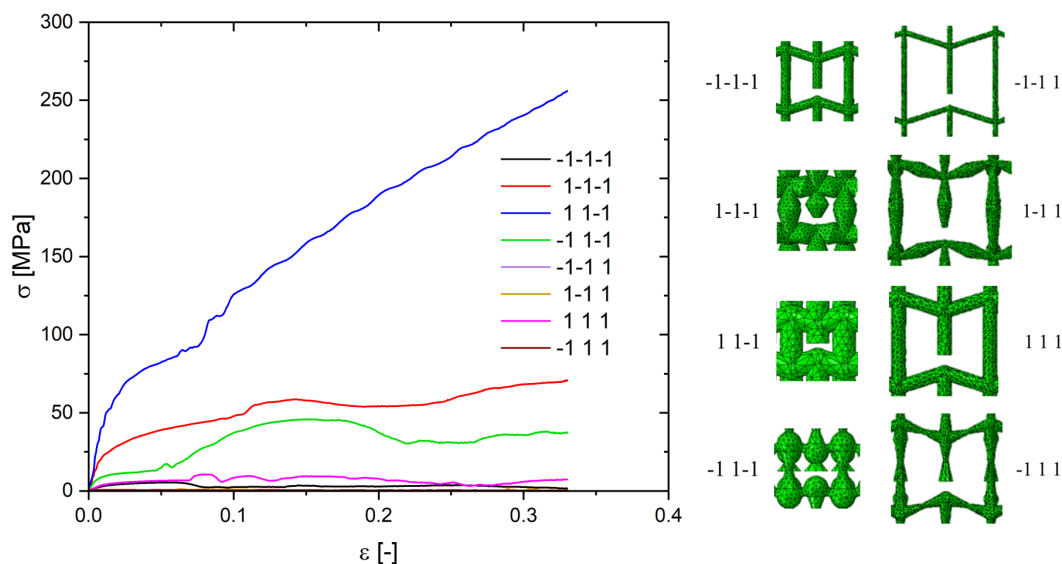
Figure 8. Simulated stress–strain diagrams of all eight variants. 1 and -1 denote to the max and min value of the three geometry parameters waist, strut thickness, and size, respectively. Unit cells on the right for the eight variants.

ADVANCED
SCIENCE NEWS

www.advancedsciencenews.com

ADVANCED
ENGINEERING
MATERIALS

www.aem-journal.com

Figure 9. a) Effect plots of the geometry parameters on the energy absorption capacity E and Poisson's ratio ν. The optimization of E opposes the optimization of Poisson's ratio. b) Effect plots of the product $E \cdot \nu$.

3.3. Quasistatic Compression Experiments

The quasistatic compression experiments display good accordance with the FE simulations until the first PCS (**Figure 10**). After that, all structures failed brittle, which was not accounted for in the simulations. Therefore, microtensile tests on single struts are necessary in the future for better material model calibration. Further noticeable is the increase in the PCS for the smaller structures compared with the larger structures. However, for the structures with straight struts, it is only an increase by a factor of ≈ 14; the structures with waist and belly increase their PCS by a factor of ≈ 50.

In addition, the large structures did not reach the contact point because they sheared off during plastic deformation instead of collapsing in a straight fashion (**Figure 11**, $\epsilon = 7.8\%$). Also a bending-dominated deformation mechanism becomes visible for the experiments, especially for the large structures. That is the reason why the simulations for the smaller structures are better match for the experiments. The smaller structures also display a shearing off (**Figure 12**), but as the struts are smaller, the bending is not as dominant. Shearing off is another reason as to why the calculation of Poisson's ratio is only valid before an initial failure of the specimen. The simulations of the larger structures further display an oscillating behavior after the PCS (Figure 10e–h). The respective maxima are points of contact during deformation, followed by a gliding of the half struts and a sudden collapse of one layer (Figure 11, simulation). The smaller structures do not show this behavior because there is not as much space for gliding of the half struts as it is for the large structures.
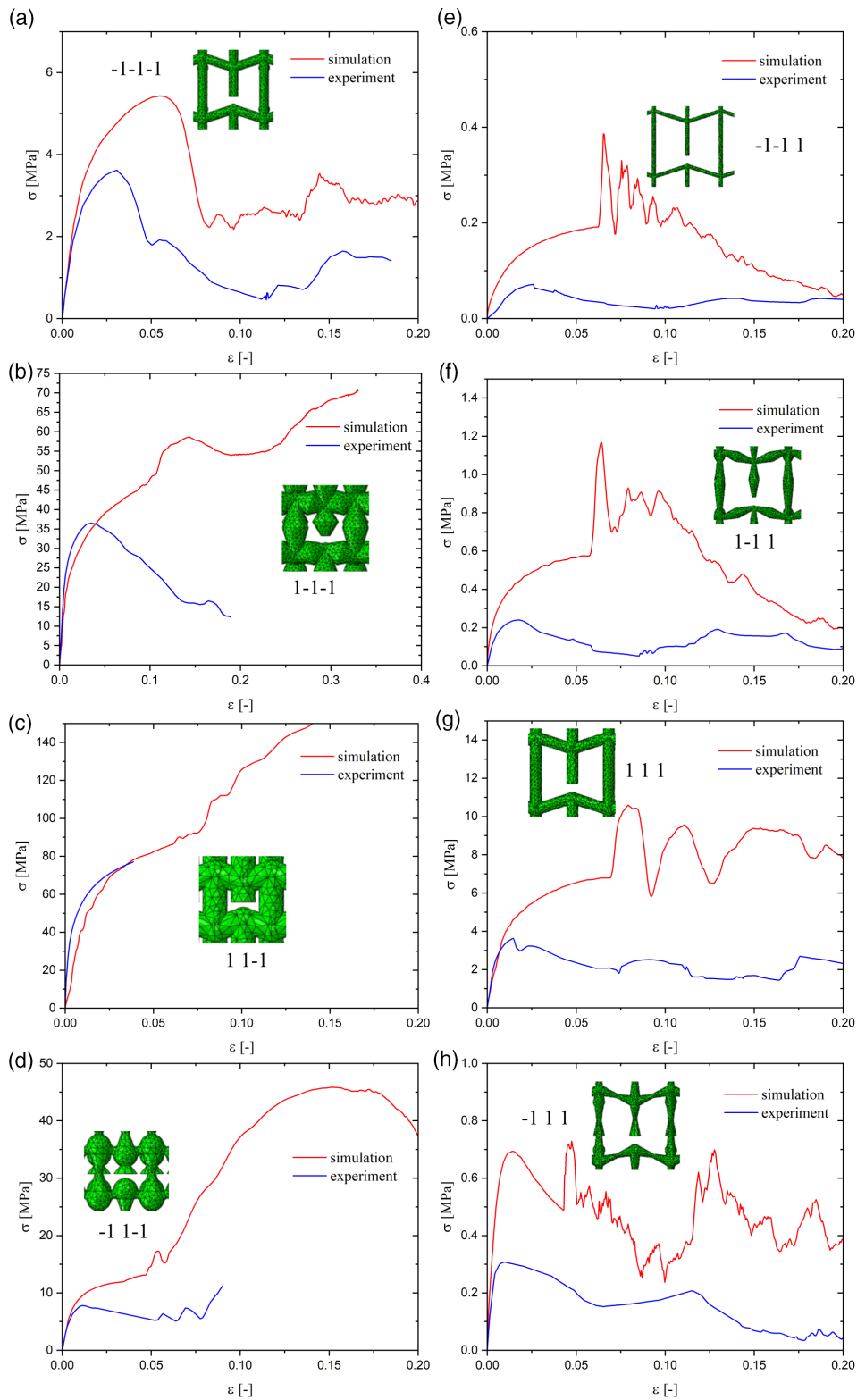
Even though the material model of the simulation was based on preceding tensile tests of SLM-manufactured aluminum, the material parameters of the later-manufactured auxetic structures may differ because of high process complexity. Those are also the reasons as to why the measured Poisson's ratios (**Table 5**) slightly differ from the predicted values. The simulations overestimate the negative Poisson's ratios for the larger structures. For the

smaller structures, the Poisson's ratios are underestimated by the simulations with the exception of the structure with waited struts $(-1\ 1\ -1)$. However, the overall tendencies of the Poisson's ratio stay the same as in the simulations. The comparison of the energy absorption capacity up to 5% strain (Table 5) also confirms the best compromise being a small structure with a waist $(-1\ 1\ -1)$. It also shows the better match of the simulations for the small structures compared with large structures. As the compromise was verified by the experiments and the overall tendencies were kept, the simulations are applicable for an optimization. They give a good estimate as to how the geometry parameters influence the overall behavior of the structures. With an optimization of the AM process, the experiments and the simulations would be a better match, but due to the high process complexity, this is beyond the scope of this contribution.

4. Conclusion

The FE simulations show the high tailoring potential of the auxetic structures. With only three geometry parameters, a wide range of stress−strain behavior as well as Poisson's ratios is achievable. From the factorial testing plan, it also becomes clear that the unit cell size is the geometry parameter with the biggest impact. In addition, an optimization of both energy absorption capacity and Poisson's ratio is not straightforward because the geometry parameters have an opposing effect on the two target values. To find a good compromise, a minimization of the product of energy absorption capacity and Poisson's ratio is a first, simple approach.

The quasistatic compression experiments proved good accordance of simulation and manufactured specimens up to the first PCS. As SLM is a highly complex manufacturing process with many parameters and varying heat removal during fabrication, the aluminum properties vary from specimen type to specimen type. Therefore, the simulations overestimate the stresses and consequently the energy absorption capacity. The simulations did additionally not account for brittle failure, which was the case for most

ADVANCED
SCIENCE NEWS
www.advancedsciencenews.com

ADVANCED
ENGINEERING
MATERIALS
www.aem-journal.com

Figure 10. Stress−strain diagrams of the simulations compared with the experiments. All experimental curves are the mean value of three experiments. The geometry parameters are according to Table 1. a−d) The small structures are on the left and the e−h) large structures on the right.
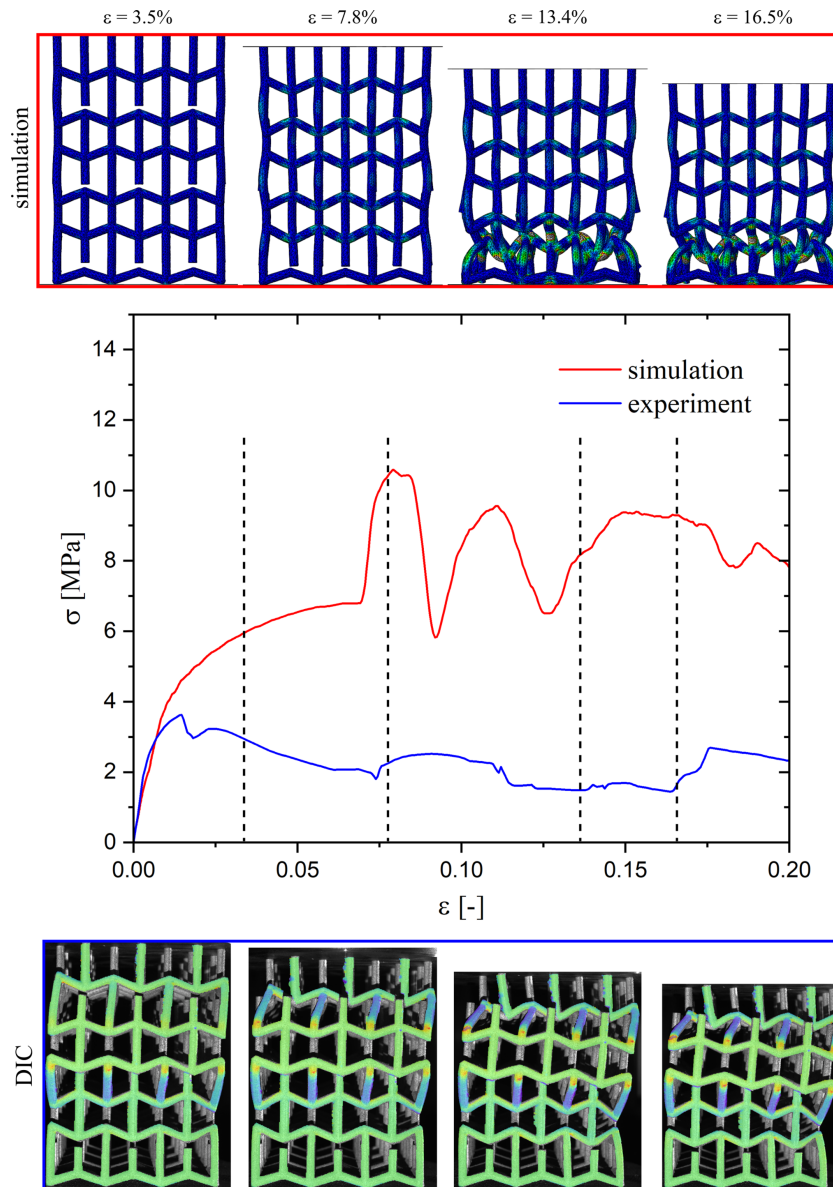
Figure 11. Comparison of the deformation behavior between simulation and experiment for specific global strains ϵ on the example of the large structure with all geometry parameters on maximum level (1 1 1).
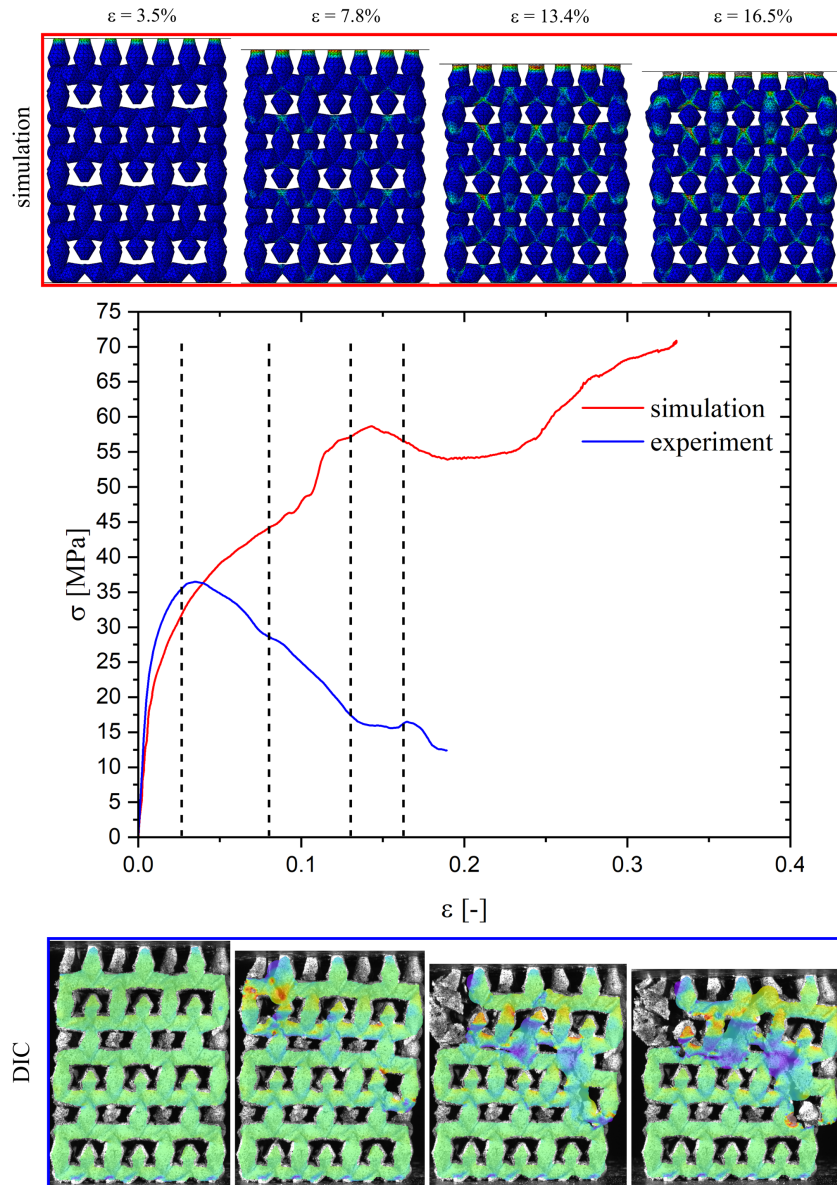
specimens. This in combination with a shearing off of the manufactured structures leads to deviation of the predicted Poisson's ratios to the experimentally calculated ones. Nevertheless, the overall predicted tendencies could be seen. Especially among the small structures were two with positive Poisson's ratio and therefore the auxetic effect was lost. Hence, even with a re-entrant honeycomb microstructure, an auxetic effect is not guaranteed.

The point of contact, predicted in the simulations, is not as clearly displayed in the experiments. Responsible is the shearing off, visible in the DIC. The half struts cannot go down in a straight fashion and therefore glide and bend instead of bearing the load. The bending-dominant failure is another reason for the overestimation of the simulations. As there are inhomogeneities within the

specimens, the single struts are much more prone to buckle and therefore fail under less load than without buckling. For the larger specimens, this buckling is more dominant than for the smaller ones. Therefore, the deviations are higher for the bigger structures.

However, this contribution showed the high tailoring potential of re-entrant, modified honeycomb structures with just three simple geometry parameters. Moreover, the impact of the unit cell size was demonstrated to be the most influential factor on both energy absorption capacity and Poisson's ratio. The experimental analysis of all structures verified the simulations until the PCS and pointed out the bending-dominated failure mechanism of the SLM-manufactured specimens. Poisson's ratios up to -0.51 were reached in the experiments, showing a high auxetic effect. The strut

**ADVANCED
SCIENCE NEWS**

www.advancedsciencenews.com

**ADVANCED
ENGINEERING
MATERIALS**

www.aem-journal.com

Figure 12. Comparison of the deformation behavior between simulation and experiment for specific global strains ε on the example of the small structure with a belly $(1 - 1 - 1)$.

Table 5. Experimental (exp) and simulated (sim) Poisson's ratio ν and energy absorption capacity E up to 5% strain for the eight parameter sets, with their respective errors e. -1 and 1 represent the min and max value of the three geometry parameters waist, strut thickness, and size, respectively. Marked in green is the best compromise solution for the experiment, which is the same as for the simulations.

	Parameter level	ν_{exp} [$-$]	ν_{sim} [$-$]	e_ν [$-$]	E_{exp} [mJ mm^{-3}]	E_{sim} [mJ mm^{-3}]	e_E [$-$]
Small	$-1-1-1$	-0.40	-0.33	0.175	0.137	0.201	0.31
	$1-1-1$	0.13	0.03	0.76	1.564	1.456	0.07
	$1\ 1-1$	0.16	0.01	0.94	3.443	3.246	0.06
	$-1\ 1-1$	-0.22	-0.45	1.05	0.313	0.529	0.41
Large	$-1-1\ 1$	-0.51	-0.64	0.25	0.002	0.007	0.71
	$1-1\ 1$	-0.40	-0.67	0.68	0.009	0.022	0.59
	$1\ 1\ 1$	-0.36	-0.44	0.22	0.141	0.249	0.43
	$-1\ 1\ 1$	-0.34	-0.41	0.21	0.013	0.029	0.55

thickness is the geometry parameter with the smallest influence for optimization purposes. Thus, for a feature reduction, the strut thickness does not need to be varied as much as the other two parameters. Consequently, the amount of generated training for structural optimization by machine learning applications can be reduced.

Conflict of Interest

The authors declare no conflict of interest.

Data Availability Statement

Research data are not shared.

[1] R. Lakes, *Nature* **1992**, *358*, 713.

[2] T.-C. Lim, *Mech. Adv. Mater. Struct.* **2015**, *22*, 205.

[3] M. Bianchi, F. Scarpa, C. Smith, *Acta Mater.* **2010**, *58*, 858.

[4] R. Lakes, *J. Mech. Des.* **1993**, *115*, 696.

[5] K. L. Alderson, V. R. Simkins, V. L. Coenen, P. J. Davies, A. Alderson, K. E. Evans, *Phys. Status Solidi (b)* **2009**, *242*, 509.

[6] R. Lakes, *Science* **1987**, *235*, 1038.

[7] R. Lakes, K. Elms, *J. Compos. Mater.* **1993**, *27*, 1193.

[8] N. Novak, M. Vesenjak, Z. Ren, *Sci. Technol. Mater.* **2018**, *30*, 4.

[9] G. Imbalzano, S. Linforth, T. D. Ngo, P. V. S. Lee, P. Tran, *Compos. Struct.* **2018**, *183*, 242.

[10] N. Novak, L. Starčevič, M. Vesenjak, Z. Ren, *Compos. Struct.* **2019**, *210*, 167.

[11] K. K. Dudek, W. Wolak, R. Gatt, J. N. Grima, *Sci. Rep.* **2019**, *9*, 1.

[12] A. Bezazi, F. Scarpa, *Int. J. Fatigue* **2007**, *29*, 922.

[13] F. Scarpa, P. Pastorino, A. Garelli, S. Patsias, M. Ruzzene, *Phys. Status Solidi (B)* **2005**, *242*, 681.

[14] T. Fíla, P. Koudelka, J. Falta, P. Zlámal, V. Rada, M. Adorna, S. Bronder, O. Jiroušek, *Int. J. Impact Eng.* **2020**, *148*, 103767.

[15] A. Mauko, T. Fla, J. Falta, P. Koudelka, V. Rada, M. Neuhäuserová, P. Zlámal, M. Vesenjak, O. Jiroušek, Z. Ren, *Metals* **2021**, *11*, 52.

[16] N. Novak, M. Vesenjak, S. Tanaka, K. Hokamoto, Z. Ren, *Int. J. Impact Eng.* **2020**, *141*, 103566.

[17] L. Mizzi, A. Spaggiari, *Smart Mater. Struct.* **2020**, *29*, 105036.

[18] S. Bronder, M. Adorna, T. Fíla, P. Koudelka, J. Falta, O. Jiroušek, A. Jung, *Adv. Eng. Mater.* **2021**, *23*, 2001393.

[19] J. Choi, R. Lakes, *Cell. Polym.* **1991**, *10*, 205.

[20] B. Caddock, K. Evans, *Biomaterials* **1995**, *16*, 1109.

[21] L. Foster, P. Peketi, T. Allen, T. Senior, O. Duncan, A. Alderson, *Appl. Sci.* **2018**, *8*, 354.

[22] J. Clarke, R. Duckett, P. Hine, I. Hutchinson, I. Ward, *Composites* **1994**, *25*, 863.

[23] C. T. Herakovich, *J. Compos. Mater.* **1984**, *18*, 447.

[24] A. Alderson, K. Alderson, *Proc. Inst. Mech. Eng., Part G: J. Aerospace Eng.* **2007**, *221*, 565.

[25] K. Alderson, A. Alderson, G. Smart, V. Simkins, P. Davies, *Plastics Rubber Compos.* **2002**, *31*, 344.

[26] V. Gorodtsov, D. Lisovenko, *Mech. Solids* **2020**, *55*, 461.

[27] D. Veronda, R. Westmann, *J. Biomech.* **1970**, *3*, 111.

[28] L. Frolich, M. Labarbera, W. Stevens, *J. Zool.* **1994**, *232*, 231.

[29] C. Lees, J. F. Vincent, J. E. Hillerton, *Bio-med. Mater. Eng.* **1991**, *1*, 19.

[30] K. E. Evans, M. Nkansah, I. Hutchinson, S. Rogers, *Nature* **1991**, *353*, 124.

[31] R. Almgren, *J. Elast.* **1985**, *15* 427.

[32] J. N. Grima, K. E. Evans, *J. Mater. Sci. Lett.* **2000**, *19*, 1563.

[33] W. Wu, D. Qi, H. Liao, G. Qian, L. Geng, Y. Niu, J. Liang, *Sci. Rep.* **2018**, *8*, 1.

[34] W. Wu, W. Hu, G. Qian, H. Liao, X. Xu, F. Berto, *Mater. Des.* **2019**, *180*, 107950.

[35] K. Dudek, A. Drzewiński, M. Kadic, *Proc. R. Soc. A* **2021**, *477*, 20200825.

[36] L. Mizzi, A. Spaggiari, *Mech. Mater.* **2021**, *153*, 103698.

[37] H. Yang, B. Wang, L. Ma, *Int. J. Solids Struct.* **2019**, *180*, 13.

[38] S. Bronder, S. Diebels, A. Jung, *PAMM* **2021**, *20*, e202000238.

[39] W. Meiners, K. Wissenbach, A. Gasser, German Patent 19 649, **1998**.

[40] X. Wang, M. Jiang, Z. Zhou, J. Gou, D. Hui, *Compos. Part B: Eng.* **2017**, *110*, 442.

[41] C. Y. Yap, C. K. Chua, Z. L. Dong, Z. H. Liu, D. Q. Zhang, L. E. Loh, S. L. Sing, *Appl. Phys. Rev.* **2015**, *2*, 041101.

[42] R. Singh, in *Advanced Materials Research*, Vol. *83*, **2010**, pp. 342–349.

[43] W. Wu, D. Qi, W. Hu, L. Xi, L. Sun, B. Liao, F. Berto, G. Qian, D. Xiao, *Mater. Des.* **2020**, *192*, 108743.

[44] D. Qi, W. Hu, K. Xin, Q. Zeng, L. Xi, R. Tao, H. Liao, Y. Deng, B. Liao, W. Wu, *Compos. Struct.* **2020**, *252*, 112710.

[45] W. Hu, X. Cao, X. Zhang, Z. Huang, Z. Chen, W. Wu, L. Xi, Y. Li, D. Fang, *Extreme Mech. Lett.* **2021**, *44*, 101229.

[46] K. Siebertz, D. van Bebber, T. Hochkirchen, *Versuchspläne*, Springer, Berlin Heidelberg **2010**.

[47] DIN EN ISO 6892-1, *Metallische Werkstoffe—Zugversuch—Teil 1: Prüfverfahren bei Raumtemperatur*, Beuth, Berlin **2017**.